ANALYSIS OF A QUADRUPLE CORNER-CUT RIDGED/VANE-LOADED CIRCULAR WAVEGUIDE USING SCALED BOUNDARY FINITE ELEMENT METHOD

J. Liu and G. Lin

Faculty of Infrastructure Engineering
Dalian University of Technology, Dalian 116024, China

Abstract—This paper presents an extension of the recently-developed efficient semi-analytical method, namely scaled boundary finite element method (SBFEM) to analyze quadruple corner-cut ridged circular waveguide. Owing to its symmetry, only a quarter of its cross-section needs to be considered. The entire computational domain is divided into several sub-domains. Only the boundaries of each sub-domain are discretized with line elements leading to great flexibility in mesh generation, and a variational approach is used to derive the scaled boundary finite element equations. SBFEM solution converges in the finite element sense in the circumferential direction, and more significantly, is analytical in the radial direction. Consequently, singularities around re-entrant corners can be represented exactly and automatically. By introducing the "dynamic stiffness" of waveguide, using the continued fraction solution and introducing auxiliary variables, a generalized eigenvalue equation with respect to wave number is obtained without introducing an internal mesh. Numerical results illustrate the accuracy and efficiency of the method with very few elements and much less consumed time. Influences of corner-cut ridge dimensions on the wave numbers of modes are examined in detail. The single mode bandwidth of the waveguide is also discussed. Therefore, these results provide an extension to the existing design data for ridge waveguide and are considered helpful in practical applications.

1. INTRODUCTION

Since the introduction of the ridge waveguides by Cohn in 1947 [1], they have received considerable attention, and research on them has continued steadily. Compared to the conventional rectangular waveguide, ridge waveguide possesses several unique characteristics: wider single-mode bandwidth, longer dominant cutoff wavelength, and lower impedance [1, 2]. That is why the ridge waveguide has found many practical applications in microwave and millimeter-wave devices, such as cross-guide directional coupler, ridge waveguide transition, ridge bandpass filter, etc. Early works on ridge waveguides were focused on single and double ridge rectangular waveguides. Recent works aim to develop new ridge waveguides with more complicated structure, such as rectangular waveguides with one or two T-shaped septa, two double-ridged waveguides, antipodal ridged waveguides, double antipodal ridged waveguides, quadruple-ridged waveguides and octo-ridged loaded cylindrical waveguide, etc. The properties of many ridged waveguides are well summarised by Rong and Zak [3]. As the ever-growing needs of the modern communication systems work at higher and higher capacity, many types of structures have been widely adopted in the area of microwave tubes community, such as in quadruple-ridge waveguides, magnetrons, gyrotrons, gyro-peniotrons, gyro-TWTs, etc. [4-12]. Among them, quadruple-ridge waveguides find wide applications, especially in antenna and radar systems [4, 5] because of their supporting dual-polarization capabilities. The transmission characteristics of quadruple ridged waveguides have been obtained by employing various numerical approaches including the finite element method (FEM) [13], the magnetic field integral equation (MFIE) method [14], multilayer perceptron neural network model (MLPNN) [15], mode-matching method (MMM) [16] transverse resonance technique [17], Ritz-Galerkin approach [18], boundary element method (BEM) [19], Multipole Theory (MT) [20]. In practical applications, the quadruple ridges in a square waveguide are usually cut at their corners [21] as shown in Figure 1, which contains reentrant corners.

This leads to substantially lower the cutoff frequency of the dominant mode and also to enhance the power handling capacity. It is well accepted that, among those methods, the FEM is undoubtedly the dominant method for modeling waveguide problems at present, because of its powerful capability of simulating a large variety of problems with complex structural geometries, complicated material properties, and various boundary conditions. The flexibility of the FEM would seem to make it ideally suited for the quadruple corner-
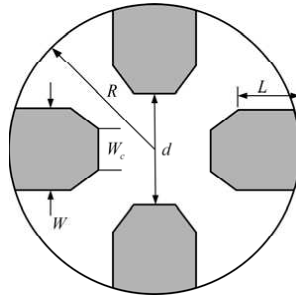
Figure 1. Cross-section of a quadruple corner-cut ridged circular waveguide.

cut ridged square waveguide. However, the standard FEM yields comparatively poor results when applied to the waveguide whose domain contains re-entrant corners, owing to the singular nature of the solution. The method used to circumvent this difficulty is to refine the mesh locally in the region of the singularity which will lead to a large computational effort, or to introduce singular elements [22], which incorporate the asymptotic singular stress functions. The BEM is an attractive technique for solving the waveguide problems, since only the boundary is discretized, which results in a reduction of the spatial dimension by one. However, fundamental solutions are required, and singular integrals exist. Furthermore, it may suffer from the problems caused by sharp corners.

Recently, a semi-analytical method called scaled boundary finite element (SBFEM) has emerged as an attractive alternative to analyze the quadruple corner-cut ridged circular waveguide. The SBFEM is a novel semi-analytical technique and has been developed to solve soil-structure interaction problems, which was proposed (1997) [23] and systematically described (2003) [24] by Wolf and Song. In recent years, further development of the method has been performed for different fields of physics, such as elastomechanics, dynamics, geomechanics, diffusion, acoustical, potential flow and electrostatic field, et cetera [25]. Its versatility, accuracy and efficiency are not only equal to, but also potentially better than the finite element method and the boundary element method for certain problems. The SBFEM weakens the governing differential equation in the circumferential direction and solves the weakened equation analytically in the radial direction so that the modeled spatial dimensions are reduced by one as the BEM, and meanwhile it does not need fundamental solutions as the FEM. Besides, it presents appealing features of its own such as no discretization of side-face boundaries so that the

computation cost can be further reduced and representing singularities and unbounded domains accurately, etc. [24]. Meanwhile, no internal mesh is required as a generalized eigenvalue equation is established by introducing the "dynamic stiffness" of waveguide, using the continued fraction solution and introducing auxiliary variables [26]. Nowadays, there are several approaches to derive the governing equations of SBFEM, i.e., the mechanically-based derivation [24], weighted residual formulation [24], virtual work principle formulation [27] and Hamiltonian-based derivation [28] respectively. A variational approach for the formulation of SBFEM governing equation of the waveguide eigenvalue problems is proposed in this paper, because the functional with respect to the waveguide eigenvalue problems based on the two-dimensional Helmholtz wave equation can be easily constructed and easy to understand.

The further outline of this paper is as follows: In Section 2, the concept and fundamental equations of SBFEM for the waveguide problems are summarized. In Section 3, the dynamic stiffness equation for waveguide wave is formulated and a generalized eigenvalue equation is constructed using the continued fraction technique. In Section 4, the normalized wave numbers of the dominant and the first 20 wave higher-order modes for both TE and TM cases, which are seldom reported in the literature especially for TM case, are calculated. The accuracy and efficiency of the method are checked. Then, the effect of quadruple corner-cut ridges in the circular waveguide is examined. The single-mode bandwidth can then be evaluated by comparing the dominant and TE_{21U} or TE_{31} modes. A discussion and conclusions follow in Section 5.

2. SCALED BOUNDARY FINITE ELEMENT METHOD FOR WAVEGUIDE PROBLEMS

The functional expression with respect to the waveguide eigenvalue problems based on the two-dimensional Helmholtz wave equation can be easily constructed as follows

$$\delta F\left(\varphi\right) = \delta\left(\frac{1}{2}\int_{\Omega}\left[\left(\frac{\partial\varphi}{\partial x}\right)^2 + \left(\frac{\partial\varphi}{\partial y}\right)^2 - k_c^2\varphi^2\right]d\Omega\right) = 0 \qquad (1)$$

where φ is the longitudinal field components, and k_c is the wave number. For the TM case, $\varphi = E_z$. The variable φ satisfies the homogeneous Dirichlet boundary condition $\varphi = 0$ on the whole boundary. Whereas for the TE case, $\varphi = H_z$, φ meets the homogeneous Neumann boundary condition $\frac{\partial\varphi}{\partial\tilde{n}} = 0$.
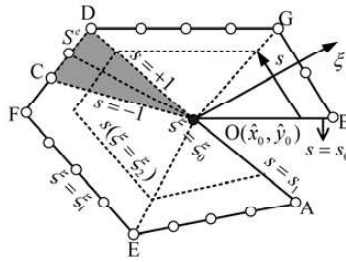
Figure 2. The coordinate definition of SBFEM.

To apply the SBFEM to Equation (1) for two-dimensional problems, the so-called scaled boundary coordinate system is introduced. A typical scaled boundary coordinate system is shown in Figure 2.

A domain is represented by scaling a defining curve S relative to a scaling center $O(\hat{x}_0, \hat{y}_0)$. The scaling center (Figure 2 with node shown as solid dot) is chosen such that the whole boundary is visible from it (In case of geometries where it is not possible to find such a scaling center, the entire geometry is sub-structure, and in each sub-structure the scaling center can be chosen, and the SBFEM can be applied to each sub-structure independently and combined together so that in effect the whole geometry is analyzed). The boundary is divided into line elements (Figure 2 with nodes shown as hollow circles). The circumferential coordinate s is anticlockwise along the boundary curve S, and the normalized radial coordinate ξ represents a scaling factor, defined as 1 at the boundary S and O at the scaling center. For the domain studied in this problem, the whole solution domain Ω is in the range of $0 = \xi_0 \leq \xi \leq \xi_1 = 1$ and $s_0 \leq s \leq s_1$. The shaded area shows the region resulting from scaling a typical element on S. A point $(\hat{x}, \hat{y})$ inside the domain, which is mapped between this coordinate system and the Cartesian coordinate system, can be expressed as follows

$$\hat{x} = \hat{x}_0 + \xi x(s) = \hat{x}_0 + \xi \mathbf{N}(s)\mathbf{x}; \quad \hat{y} = \hat{y}_0 + \xi y(s) = \hat{y}_0 + \xi \mathbf{N}(s)\mathbf{y}$$

where $\mathbf{N}(s)$ is the shape function; $(x(s), y(s))$ is an arbitrary point on the boundary S; $(\hat{x}, \hat{y})$ is an interior point of the domain.

The spatial derivatives in the two coordinate systems are related as

$$\left\{ \begin{array}{c} \frac{\partial}{\partial \hat{x}} \\ \frac{\partial}{\partial \hat{y}} \end{array} \right\} = \hat{\mathbf{J}}(\xi, s) \left\{ \begin{array}{c} \frac{\partial}{\partial \xi} \\ \frac{\partial}{\partial s} \end{array} \right\} = \frac{1}{|J|} \left[\begin{array}{cc} y(s)_{,s} & -y(s) \\ -x(s)_{,s} & x(s) \end{array} \right] \left\{ \begin{array}{c} \frac{\partial}{\partial \xi} \\ \frac{1}{\xi} \frac{\partial}{\partial s} \end{array} \right\}$$

with the Jacobian matrix defined as

$$\hat{\mathbf{J}}\left(\xi,s\right)=\begin{bmatrix}\hat{x}_{,\xi}&\hat{y}_{,\xi}\\\hat{x}_{,s}&\hat{y}_{,s}\end{bmatrix}=\begin{bmatrix}1&0\\0&\xi\end{bmatrix}\begin{bmatrix}y(s)_{,s}&-y(s)\\-x(s)_{,s}&x(s)\end{bmatrix}=\begin{bmatrix}1&0\\0&\xi\end{bmatrix}\mathbf{J}\left(\xi,s\right)$$

and

$$|J| = x(s)y(s)_{,s} - y(s)x(s)_{,s}$$

The infinitesimal area of the domain can be calculated as

$$d\Omega = \xi\left|J\right|d\xi ds \tag{2}$$

The Laplace operator ∇ can also be expressed as

$$\nabla = \mathbf{b}_1(s)\frac{\partial}{\partial\xi} + \frac{1}{\xi}\mathbf{b}_2(s)\frac{\partial}{\partial s} \tag{3}$$

where

$$\mathbf{b}_1(s) = \frac{1}{|J|}\left\{\begin{array}{c}y(s)_{,s}\\-x(s)_{,s}\end{array}\right\}, \quad \mathbf{b}_2(s) = \frac{1}{|J|}\left\{\begin{array}{c}-y(s)\\x(s)\end{array}\right\}$$

A typical SBFEM element S^e (superscript e for element) as the shaded part of the domain is shown in Figure 2. The same shaped function is postulated to apply to $\varphi(\xi,s)$

$$\varphi(\xi,s) = \mathbf{N}(s)\boldsymbol{\varphi}(\xi) \tag{4}$$

where vector $\boldsymbol{\varphi}\left(\xi\right)$ represents radial nodal functions analogous to nodal values.

Substituting Equations (3), (4) into Equation (1) yields

$$\delta F\left(\varphi\right) = \delta\left(\frac{1}{2}\int_{\Omega}\left(\mathbf{B}_1(s)\boldsymbol{\varphi}\left(\xi\right)_{,\xi}+\frac{1}{\xi}\mathbf{B}_2(s)\boldsymbol{\varphi}\left(\xi\right)\right)^T\left(\mathbf{B}_1(s)\boldsymbol{\varphi}\left(\xi\right)_{,\xi}\right.\right.$$

$$\left.\left.+\frac{1}{\xi}\mathbf{B}_2(s)\boldsymbol{\varphi}\left(\xi\right)\right)d\Omega-\frac{1}{2}\int_{\Omega}k_c^2\boldsymbol{\varphi}(\xi)^T\mathbf{N}(s)^T\mathbf{N}(s)\boldsymbol{\varphi}(\xi)d\Omega\right)=\mathbf{0} \tag{5}$$

with

$$\mathbf{B_1}(s) = \mathbf{b_1}(s)\mathbf{N}(s); \quad \mathbf{B_2}(s) = \mathbf{b_2}(s)\mathbf{N}(s)_{,s}$$

Expanding the left hand side of Equation (5), substituting Equations (2) into Equation (5), applying integration by parts the domain containing $\delta\boldsymbol{\varphi}\left(\xi\right)_{,\xi}$ with respect to ξ and arranging, leads to

$$\delta F\left(\varphi\right) = \delta\boldsymbol{\varphi}(\xi)^T\left(\mathbf{E}_0\xi\boldsymbol{\varphi}\left(\xi\right)_{,\xi}+\mathbf{E}_1^T\boldsymbol{\varphi}\left(\xi\right)\right)\Big|_{\xi=\xi_1=1}-\int_0^1\delta\boldsymbol{\varphi}$$

$$(\xi)^T\left(\mathbf{E}_0\left(\xi\boldsymbol{\varphi}\left(\xi\right)_{,\xi\xi}+\boldsymbol{\varphi}\left(\xi\right)_{,\xi}\right)+\mathbf{E}_1^T\boldsymbol{\varphi}\left(\xi\right)_{,\xi}-\mathbf{E}_1\boldsymbol{\varphi}\left(\xi\right)_{,\xi}-\mathbf{E}_2\frac{1}{\xi}\boldsymbol{\varphi}\left(\xi\right)\right)d\xi$$

$$-\int_0^1\delta\boldsymbol{\varphi}(\xi)^Tk_c^2\xi^2\mathbf{M}_0\boldsymbol{\varphi}(\xi)d\xi = \mathbf{0} \tag{6}$$

where

$$\mathbf{E}_0 = \int_s \mathbf{B}_1(s)^T \mathbf{B}_1(s) \, |J| \, ds; \quad \mathbf{E}_1 = \int_s \mathbf{B}_2(s)^T \mathbf{B}_1(s) \, |J| \, ds;$$

$$\mathbf{E}_2 = \int_s \mathbf{B}_2(s)^T \mathbf{B}_2(s) \, |J| \, ds; \quad \mathbf{M}_0 = \int_s \mathbf{N}(s)^T \mathbf{N}(s) \, |J| \, ds$$

Since Equation (6) should be satisfied for any set of function $\delta\boldsymbol{\varphi}(\xi)$, the following conditions must be met.

$$\left(\mathbf{E}_0\xi^2\boldsymbol{\varphi}(\xi)_{,\xi\xi} + \xi(\mathbf{E}_0 + \mathbf{E}_1^T - \mathbf{E}_1)\,\boldsymbol{\varphi}(\xi)_{,\xi} - \mathbf{E}_2\boldsymbol{\varphi}(\xi) + k_c^2\mathbf{M}_0\boldsymbol{\varphi}(\xi) = \mathbf{0} \quad (7)\right.$$

$$\left. \mathbf{E}_0\xi\boldsymbol{\varphi}(\xi)_{,\xi} + \mathbf{E}_1^T\boldsymbol{\varphi}(\xi)\right|_{\xi=\xi_1=1} = \mathbf{0} \quad (8)$$

Equation (7) represents the SBFEM equation and is a system of second-order ordinary differential equations for function $\boldsymbol{\varphi}(\xi)$. Equation (8) represents the boundary condition. Equations (7) and (8)) apply to the domain of the triangle (the typical SBFEM element which is the shaded part shown in Figure 2) corresponding to one finite element on the boundary, then the coefficient matrices $\mathbf{E}_0$, $\mathbf{E}_1$, $\mathbf{E}_2$, $\mathbf{M}_0$ are assembled into the whole structure, as in the standard finite element method, from the element coefficient matrices.

3. FORMULATION OF THE GENERALIZED EIGENVALUE EQUATION FOR WAVEGUIDE

To solve the differentials Equation (7), it is convenient to introduce the concept of the "dynamic stiffness" $\mathbf{S}(k_c, \xi)$. For a homogeneous waveguide wave, the dynamic stiffness $\mathbf{S}(k_c, \xi)$ relates the Fourier transform of the external nodal flux $\mathbf{R}(\xi)$ to the Fourier transform of the function $\boldsymbol{\varphi}(\xi)$ is as follows

$$\mathbf{R}(\xi) = \mathbf{S}(k_0, \xi)\boldsymbol{\varphi}(\xi) \quad (9)$$

Similar to Equation (8) on the boundary, the internal nodal flux along radial lines is equal to external nodal flux $\mathbf{R}(\xi)$ with respect to arbitrary ξ as follows

$$\mathbf{R}(\xi) = \mathbf{S}(k_0, \xi)\boldsymbol{\varphi}(\xi) = \mathbf{E}_0\xi\boldsymbol{\varphi}(\xi)_{,\xi} + \mathbf{E}_1^T\boldsymbol{\varphi}(\xi) \quad (10)$$

Multiplied by ξ after differentiating Equation (10) with respect to ξ, then adding Equation (7) results in

$$\xi\mathbf{S}(k_c, \xi)_{,\xi}\,\boldsymbol{\varphi}(\xi) + (\mathbf{S}(k_c, \xi) - \mathbf{E}_1)\,\xi\boldsymbol{\varphi}(\xi)_{,\xi} - \mathbf{E}_2\boldsymbol{\varphi}(\xi) + k_c^2\mathbf{M}_0\xi^2\boldsymbol{\varphi}(\xi) = \mathbf{0} \quad (11)$$

Solving Equation (10) for $\xi\boldsymbol{\varphi}(\xi)_{,\xi}$ and substituting in Equation (11) yields

$$\left((\mathbf{S}\left(k_c,\xi\right)-\mathbf{E}_1\right)\mathbf{E}_0^{-1}\left(\mathbf{S}\left(k_c,\xi\right)-\mathbf{E}_1^T\right)+\xi\mathbf{S}\left(k_c,\xi\right)_{,\xi}-\mathbf{E}_2+k_c^2\xi^2\mathbf{M}_0\right)\boldsymbol{\varphi}\left(\xi\right)$$
$$= \mathbf{0} \tag{12}$$

Since the equation $\xi\mathbf{S}\left(k_c,\xi\right)_{,\xi} = k_c\mathbf{S}\left(k_c,\xi\right)_{,k_c}$ can be derived in [24] and equation (12) should be satisfied for any set of variable $\boldsymbol{\varphi}(\xi)$, the dynamic stiffness $\mathbf{S}\left(k_c,\xi=1\right)$ on the boundary can be expressed (For convenience, $\mathbf{S}\left(k_c,\xi=1\right)$ is abbreviated as $\mathbf{S}\left(k_c\right)$)

$$\left(\mathbf{S}\left(k_c\right)-\mathbf{E}_1\right)\mathbf{E}_0^{-1}\left(\mathbf{S}\left(k_c\right)-\mathbf{E}_1^T\right)+k_c\mathbf{S}\left(k_c\right)_{,k_c}-\mathbf{E}_2+k_c^2\mathbf{M}_0=\mathbf{0} \tag{13}$$

Equation (13) presents the scaled boundary finite element equation in dynamic stiffness for waveguide wave. Equation (13) differs from the SBFEM equation in dynamic stiffness for elastodynamics[26] in the variable k_c instead of variable ω only. A continued fraction solution of first-order ordinary differential Equation (13) has been derived by Song (2009) [26]. So for the waveguide wave problem, the stiffness matrix $\mathbf{S}\left(k_c\right)$ can also be expanded into (introducing to $x=-k_c^2$)

$$\mathbf{S}\left(x\right) = \mathbf{K} + x\mathbf{M} - x^2\left(\mathbf{S}^{(1)}\left(x\right)\right)^{-1} \tag{14}$$

Here, the symbol $\mathbf{S}^{(1)}\left(x\right)$ denotes a yet undetermined function of x. The matrices $\mathbf{K}$, $\mathbf{M}$ and the term $\mathbf{S}^{(1)}\left(x\right)$ are determined by substituting the stiffness representation (14) in equation (13), sorting terms in descending order of powers of x and setting the terms corresponding to x^2, x and the remaining terms equal to zero. $\mathbf{S}^{(1)}\left(x\right)$ is decomposed as follows:

$$\mathbf{S}^{(1)}\left(x\right) = \mathbf{S}_0^1 + x\mathbf{S}_1^1 - x^2\mathbf{S}^{(2)}\left(x\right)^{-1} \tag{15}$$

or more general,

$$\mathbf{S}^{(i)}\left(x\right) = \mathbf{S}_0^i + x\mathbf{S}_1^i - x^2\mathbf{S}^{(i+1)}\left(x\right)^{-1} \quad (i=2,3,\ldots M_{cf}) \tag{16}$$

A continued-fraction expansion of order M is terminated after $(i=1,2,\ldots M_{cf})$ steps with the assumption $\mathbf{S}^{(M_{cf}+1)}\left(x\right) = \mathbf{0}$. The resulting continued-fraction expansion of the dynamic stiffness can be written as

$$\mathbf{S}\left(x\right) = \mathbf{K} + x\mathbf{M} - \cfrac{x^2}{\mathbf{S}_0^{(1)}+x\mathbf{S}_1^{(1)}-\cfrac{x^2}{\mathbf{S}_0^{(2)}+x\mathbf{S}_1^{(2)}-\cdots\cfrac{x^2}{\mathbf{S}_0^{(M_{cf})}+x\mathbf{S}_1^{(M_{cf})}}}} \tag{17}$$

where $\mathbf{K}$, $\mathbf{M}$, $\mathbf{S}_0^{(i)}$ and $\mathbf{S}_1^{(i)}$ $(i = 1, 2, \ldots M_{cf})$ are coefficient matrices determined recursively. The algorithm for the calculation of the coefficient matrices is summarized below (For a detailed derivation the reader is referred to [26].)

(1). Perform the real Schur decomposition in Equation (18)

$$\begin{bmatrix} \mathbf{E}_0^{-1}\mathbf{E}_1^T & -\mathbf{E}_0^{-1} \\ -\mathbf{E}_0 + \mathbf{E}_1\mathbf{E}_0^{-1}\mathbf{E}_1^T & -\mathbf{E}_1\mathbf{E}_0^{-1} \end{bmatrix} \begin{bmatrix} \mathbf{V}_{11} & \mathbf{V}_{12} \\ \mathbf{V}_{21} & \mathbf{V}_{22} \end{bmatrix}$$
$$= \begin{bmatrix} \mathbf{V}_{11} & \mathbf{V}_{12} \\ \mathbf{V}_{21} & \mathbf{V}_{22} \end{bmatrix} \begin{bmatrix} \mathbf{S}_{11} & \mathbf{S}_{12} \\ 0 & \mathbf{S}_{22} \end{bmatrix} \tag{18}$$

(2). Calculate the matrix $\mathbf{K}$

$$\mathbf{K} = \mathbf{V}_{21}\mathbf{V}_{11}^{-1}$$

(3). Solve Lyapunov Equation (19) for the matrix $\mathbf{m}$.

$$\left(\mathbf{I} - \mathbf{S}_{11}^T\right)\mathbf{m} + \mathbf{m}\left(\mathbf{I} - \mathbf{S}_{11}\right) = \mathbf{V}_{11}^T\mathbf{M}_0\mathbf{V}_{11} \tag{19}$$

Then, calculate the matrix $\mathbf{M} = \mathbf{V}_{11}^{-T}\mathbf{m}\mathbf{V}_{11}^{-1}$.

(4). Initialize the following recursive coefficient matrices:

$$\mathbf{a}^{(1)} = \mathbf{E}_0^{-1}$$
$$\mathbf{V}^{(1)} = \mathbf{V}_{11}$$
$$\mathbf{U}^{(1)} = 2\mathbf{I} - \mathbf{S}_{11}$$
$$\mathbf{b}_0^{(1)} = \mathbf{V}^{(1)}\mathbf{V}^{(1)}\left(\mathbf{V}^{(1)}\right)^{-1}$$
$$\mathbf{b}_1^{(1)} = \mathbf{E}_0^{-1}\mathbf{M}$$
$$\mathbf{c}^{(1)} = \mathbf{M}\mathbf{E}_0^{-1}\mathbf{M}$$

(5). For $i = 1, 2, \ldots M_{cf}$:

(a). Solve Lyapunov Equation (20) for the matrix $\mathbf{Y}_0^i$,

$$\mathbf{Y}_0^i\mathbf{U}^{(i)} + \left(\mathbf{U}^{(i)}\right)^T\mathbf{Y}_0^i = \left(\mathbf{V}^{(i)}\right)^T\mathbf{c}^{(i)}\mathbf{V}^{(i)} \quad . \tag{20}$$

(b). Calculate the matrix $\mathbf{S}_0^i$ with $\left(\mathbf{S}_0^i\right)^{-1} = \left(\mathbf{V}^{(i)}\right)^{-T}\mathbf{Y}_0^i\left(\mathbf{V}^{(i)}\right)^{-1}$.

(c). Solve Lyapunov Equation (21) for the matrix $\mathbf{Y}_1^i$,

$$\left(\mathbf{I} + \left(\mathbf{U}^{(i)}\right)^T\right)\mathbf{Y}_1^i + \mathbf{Y}_1^i\left(\mathbf{I} + \mathbf{U}^{(i)}\right)$$
$$= \left(V^{(i+1)}\right)^T\left(\mathbf{b}_1^i\mathbf{S}_0^i + \mathbf{S}_0^i\left(\mathbf{b}_1^i\right)^T\right)V^{(i+1)}. \tag{21}$$

(d). Calculate the matrix $\mathbf{S}_1^i$ with $\mathbf{S}_1^i = \left(\mathbf{V}^{(i+1)}\right)^{-T}\mathbf{Y}_1^i\left(\mathbf{V}^{(i+1)}\right)^{-1}$.

(e). Compute recursively:

$$\mathbf{a}^{(i+1)} = \mathbf{c}^{(i)}$$
$$\mathbf{V}^{(i+1)} = \left(S_0^{(i)}\right)^{-1}\mathbf{V}^{(i)}$$
$$\mathbf{U}^{(i+1)} = 2\mathbf{I} + \mathbf{U}^{(i)}$$
$$\mathbf{b}_0^{(i+1)} = \mathbf{V}^{(i+1)}\mathbf{U}^{(i+1)}\left(\mathbf{V}^{(i+1)}\right)^{-1}$$
$$\mathbf{b}_1^{(i+1)} = -\left(\mathbf{b}_1^{(i)}\right)^T + \mathbf{c}^{(i)}\mathbf{S}_1^{(i)}$$
$$\mathbf{c}^{(i+1)} = \mathbf{a}^{(i)} - \mathbf{b}_1^{(i)}\mathbf{S}_1^{(i)} - \mathbf{S}_1^{(i)}\left(\mathbf{b}_1^{(i)}\right)^T + \mathbf{S}_1^{(i)}\mathbf{c}^{(i)}\mathbf{S}_1^{(i)}$$

Continue.

Referred to [26], a corresponding representation of the flux-longitudinal field relationship for waveguide wave can be also obtained by introducing internal variables. Using Equation (14), the relationship between the Fourier transform of the external nodal flux $\mathbf{R}$ and the Fourier transform of the longitudinal field $\boldsymbol{\varphi}$ on the boundary can be written as

$$\mathbf{R} = \mathbf{K}\boldsymbol{\varphi} + x\mathbf{M}\boldsymbol{\varphi} - x\boldsymbol{\varphi}^{(1)} \tag{22}$$

where the auxiliary variable $\boldsymbol{\varphi}^{(1)}$ is defined as

$$x\boldsymbol{\varphi} = \mathbf{S}^{(1)}\left(x\right)\boldsymbol{\varphi}^{(1)} \tag{23}$$

Equation (23) is in the same form as the definition of the dynamic stiffness matrix in Equation (19). Denoting $\boldsymbol{\varphi}^{(0)} = \boldsymbol{\varphi}$. By introducing the other auxiliary variables $\boldsymbol{\varphi}^{(i+1)}$, Equation (24) is generalized for the ith term of the continued fraction as

$$x\boldsymbol{\varphi}^{(i-1)} = \mathbf{S}^{(i)}\left(x\right)\boldsymbol{\varphi}^{(i)} \tag{24}$$

Using Equation (16), Equation (24) is expressed as

$$-x\boldsymbol{\varphi}^{(i-1)} + \mathbf{S}_0^i\boldsymbol{\varphi}^{(i)} + x\mathbf{S}_1^i\boldsymbol{\varphi}^{(i)} - x\boldsymbol{\varphi}^{(i+1)} = \mathbf{0} \quad (i \geq 1) \tag{25}$$

This process is continued until the approximation $\boldsymbol{\varphi}^{(M_{cf}+1)} = \mathbf{0}$. By combining Equations (23) and (25), the relationship between the Fourier transforms of flux and temperature at the boundary is represented by a total of $(M_{cf} + 1)$ linear equations as follows

$$\left(\mathbf{K}_h - k_c^2\mathbf{M}_h\right)\mathbf{y} = \mathbf{f} \tag{26}$$

with symmetric matrixes $\mathbf{K}_h$ and $\mathbf{M}_h$

$$\mathbf{K}_h = \operatorname{diag}\left(\mathbf{K}, \mathbf{S}_0^{(1)}, \mathbf{S}_0^{(2)}, \ldots, \mathbf{S}_0^{(M)}\right)$$

$$\mathbf{M}_h = \begin{bmatrix} \mathbf{M} & -\mathbf{I} & \mathbf{0} & \ldots & \mathbf{0} \\ -\mathbf{I} & \mathbf{S}_1^{(1)} & -\mathbf{I} & \ldots & \mathbf{0} \\ \mathbf{0} & -\mathbf{I} & \mathbf{S}_1^{(2)} & \ldots & \mathbf{0} \\ \vdots & \vdots & \vdots & \ddots & \vdots \\ \mathbf{0} & \mathbf{0} & \mathbf{0} & \ldots & \mathbf{S}_1^{(M)} \end{bmatrix}$$

$$\mathbf{y} = \left(\boldsymbol{\varphi}, \boldsymbol{\varphi}^{(1)}, \boldsymbol{\varphi}^{(2)} \ldots \boldsymbol{\varphi}^{(M)}\right)^T$$

$$\mathbf{f} = (R, \mathbf{0}, \mathbf{0} \ldots \mathbf{0})^T$$

where $\mathbf{f}$ is the external flux vector on the boundary, and $\mathbf{y}$ consists of the longitudinal field function φ and the auxiliary variables $\boldsymbol{\varphi}^{(i)}$ $(i = 1, 2, \ldots M_{cf})$ on the boundary.

When the problem domain is divided into simpler sub-domains, the global equation of motion can be obtained by assembling the equations of motion of individual sub-domains (Equation (26)) according to the element connectivity as in the FEM. The resulting global equation of motion is denoted as

$$\left(\mathbf{K}_G - k_c^2 \mathbf{M}_G\right) \mathbf{y} = \mathbf{F} \tag{27}$$

$\mathbf{F} = \mathbf{0}$ is achieved after enforcing the boundary condition Equation (8) for a homogeneous waveguide eigenvalue problem without external source. For the TE case, the number of degrees of freedom (DOFs), which is the size of the eigenvalue problem, is $(\mathrm{M}_{cf} + 1) \times n$ (n is the number of the boundary nodes for SBFEM). For the TM case, after introducing the compulsive boundary condition $\varphi(\xi)|_{\xi = \xi_1 = 1} = \mathbf{0}$, the first nth row of vector $\mathbf{y}$ (in Equation (27)) tends to zero, and field function φ becomes known. Therefore, only the auxiliary variables $\boldsymbol{\varphi}^{(i)} 9i = 1, 2, \ldots M_{cf}$ are unknown, and number of DOFs reduces to $\mathrm{M}_{cf} \times n$.

4. NUMERICAL RESULTS

In order to analyze this structure, the whole cross-section (Figure 1) is divided into four identical parts because of its symmetrical geometry, as shown in Figure 3. The boundary conditions along the symmetrical planes can be either electric or magnetic walls.

Firstly, in order to verify the correctness and efficiency of the proposed method, the normalized wave numbers $2k_c R$ of the first
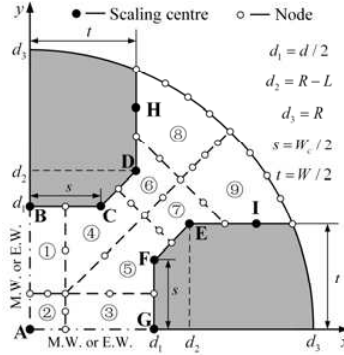
Figure 3. One quarter of the ridged corner-cut circular waveguide cross-section and SBFEM mesh.

20 higher-order modes for both TE and TM cases in a quadruple corner-cut ridged circular waveguide are calculated by SBFEM and FEM (Matlab PDE Tool). The dimensions of the ridged waveguide are $L = 0.6R$, $W = 0.4R$ and $W_c = 0.5W$. In the SBFEM, the whole domain is divided into nine sub-domains. The seventh scaling centers for the sub-domains are chosen at point A, point B, point C, point D, point E, point F, point G respectively, which may bring out singularities, and the other two scaling centers are point H and point I, as depicted in Figure 3. The three-node quadratic SBFEM element is used, which is also used throughout this paper. Three meshes are used to illustrate the convergence of the method. The coarse mesh consists of 16 elements with 33 nodes, as illustrated in Figure 3. For the TE case, the other two meshes (referred to as intermediate and fine) are constructed by binary subdivision of the coarse mesh and consist of 65 and 105 nodes, respectively (the fine model binary subdivides the intermediate model only on the circular arcs). While for the TM case, only the intermediate65 nodesand fine models105 nodesare used. The orders of continued fraction are selected as $M_{cf} = 2$ for the TE case and $M_{cf} = 3$ for the TM case, respectively. In the FEM simulation of this paper, there are also three meshes. The node numbers in the whole region of rectangular waveguide are selected as 393, 5793 and 90753, respectively. Meanwhile, the result solved by the commercially available Ansoft's High Frequency Structure Simulator (HFSS) is also used for comparison. Unfortunately, an analytical solution is not available for comparison purposes. The FEM solution whose node number is 90753 is regard as a reference. The root-mean-square error (RMSE) is defined as $error =$

Table 1. Comparison results of the wave numbers, the RMSE and the CPU times between the SBFEM and FEM.

Mode	FEM (393)	FEM (5793)	FEM (90753)	HFSS	SBFEM (33)	SBFEM (65)	SBFEM (105)	Mode	FEM (393)	FEM (5793)	FEM (90753)	SBFEM (65)	SBFEM (105)
TE11	2.3527	2.3449	2.3442	2.3457	2.3452	2.3443	2.3442	TM$_{01}$	13.9131	13.8393	13.8336	13.8347	13.8334
TE21L	2.5366	2.5265	2.5256	2.5262	2.5266	2.5257	2.5256	TM$_{11}$	14.0807	14.0306	14.0270	14.0277	14.0268
TE21U	6.3151	6.2948	6.2929	6.2930	6.2968	6.2932	6.2929	TM$_{21L}$	14.0844	14.0347	14.0311	14.0318	14.0308
TE01	7.9403	7.9315	7.9309	7.9310	7.9314	7.9309	7.9309	TM$_{21U}$	14.4547	14.3847	14.3797	14.3808	14.3798
TE31	7.9404	7.9316	7.9310	7.9311	7.9315	7.9310	7.9310	TM$_{31}$	20.8020	20.6813	20.6738	20.6743	20.6733
TE12L	7.9410	7.9322	7.9315	7.9316	7.9320	7.9315	7.9315	TM$_{02}$	20.8021	20.6813	20.6738	20.6743	20.6734
TE41	10.5331	10.5062	10.5042	10.5044	10.5091	10.5045	10.5042	TM$_{41L}$	20.8021	20.6813	20.6738	20.6743	20.6734
TE12U	11.6268	11.5912	11.5886	11.5940	11.6028	11.5893	11.5886	TM$_{12}$	21.2258	20.9957	20.9785	20.9853	20.9807
TE22L	13.2848	13.2390	13.2357	13.2360	13.2554	13.2372	13.2363	TM$_{41U}$	22.0873	21.8641	21.8472	21.8557	21.8470
TE51	14.1196	14.0783	14.0756	14.0756	14.0942	14.0768	14.0756	TM$_{22L}$	22.4288	22.2224	22.2071	22.2177	22.2080
TE22U	14.2598	14.2183	14.2157	14.2160	14.2390	14.2171	14.2157	TM$_{51}$	23.4602	23.2526	23.2385	23.2491	23.2408
TE02	14.4955	14.4477	14.4446	14.4450	14.4746	14.4466	14.4448	TM$_{22U}$	26.2171	25.8858	25.8636	25.8757	25.8641
TE32	15.8245	15.7386	15.7322	15.7323	15.7585	15.7344	15.7323	TM$_{03}$	27.2497	26.9543	26.9357	26.9400	26.9362
TE61L	17.7982	17.7111	17.7053	17.7057	17.7251	17.7066	17.7056	TM$_{32}$	27.3030	27.0113	26.9932	26.9976	26.9925
TE61U	17.8563	17.7649	17.7588	17.7591	17.7751	17.7598	17.7587	TM$_{61L}$	27.3646	27.0692	27.0509	27.0583	27.0503
TE13	17.8586	17.7676	17.7616	17.7621	17.7787	17.7626	17.7615	TM$_{61U}$	28.1993	27.8267	27.8017	27.8423	27.8203
TE71L	18.4382	18.3123	18.3030	18.3033	18.3912	18.3078	18.3028	TM$_{13}$	29.6547	29.2562	29.2294	29.2699	29.2350
TE71U	20.3553	20.2424	20.2354	20.2355	20.3272	20.2442	20.2365	TM$_{42L}$	30.4456	30.0478	30.0225	30.0346	30.0219
TE42	20.3922	20.2783	20.2712	20.2721	20.3589	20.2797	20.2718	TM$_{42U}$	30.4456	30.0482	30.0230	30.0350	30.0223
TE81L	20.3970	20.2824	20.2753	20.2762	20.3627	20.2838	20.2759	TM$_{71}$	30.4462	30.0482	30.0230	30.0351	30.0224
RMSE(%)	0.6401	0.1646	-	0.0187	0.2240	0.0186	0.0020	RMSE(%)	1.060	0.0664	-	0.0529	0.0160
Times(s)	4.61	57.95	495.57	97.58	0.23	1.47	5.53	Times(s)	4.43	53.82	463.2	1.03	4.11

$(\sum_{i=1}^{20}((k_{c\_calc} - k_{c\_FEM90753})/k_{c\_FEM90753})^2/20)^{1/2}$. The comparison results of the wave numbers, RMSE and CPU computation times (an Intel P8600 -Core 2 Duo- platform at $2.4\,\text{GHz}$ with 2-GB RAM) are given in Table 1. From the table, this method can achieve excellent accuracy and have higher efficiency with significantly fewer nodes and much less consumed time.

Then, the influence of the ridge geometry on the wave numbers of the dominant and higher-order modes for both TE and TM cases is examined and discussed as follows.

Figure 4 shows the variations of the normalized wave numbers $2k_cR$ of several lowest modes (TE modes such as TE$_{11}$, TE$_{21L}$, TE$_{21U}$, TE$_{01}$, TE$_{31}$ modes and TM modes such as TM$_{01}$, TM$_{11}$, TM$_{21L}$, TM$_{21U}$, TM$_{31}$, TM$_{02}$ modes) versus different ratio $(2R-d)/(2R)$ and different ridge thicknesses W with fixed aspect ratio $W_c/W = 0.5$.

From Figure 4, we can obtain:
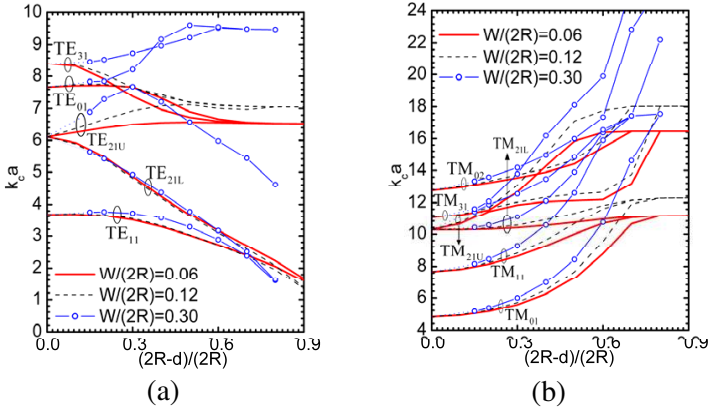
Figure 4. Normalized wave numbers versus the ridge geometry with $(2R - d)/(2R)$ and W. (a) TE modes and (b) TM modes.

For TE modes, TE_{21} mode is split into TE_{21U} and TE_{21L} modes. When the ratio $(2R-d)/(2R)$ increases with a fixed ridge thickness W, the normalized wave numbers of TE_{11} and TE_{21L} modes decrease, and the TE_{21L} mode has a wave number very close to that of the dominant symmetrical TE_{11} mode. The wave numbers of TE_{21U}, TE_{01} and TE_{31} modes tend to the same value when the ridges are heavily loaded for both $W = 0.12R$ and $W = 0.24R$. While for $W = 0.60R$, that of TE_{21U} mode increases first and then decreases, and those of the TE_{01} and TE_{31} increase and also tend to the same value as $(2R - d)/(2R)$ increases.

For the TM modes, TM_{21} mode is split into TM_{21U} and TM_{21L} modes. The normalized wave numbers of all the modes increase as the ratio $(2R-d)/(2R)$ increases with a fixed ridge thickness W, then those of TM_{01}, TM_{11} and TM_{21L} modes tend to the same value, and those of TM_{21U}, TM_{31} and TM_{02} modes have a nearly same value when the ridges are heavily loaded.

Figure 5 shows the variations of the normalized wave numbers of TE_{11}, TE_{21L}, TE_{21U}, TM_{01} and TM_{21U} modes versus different relative bigger L and different edge widths W_c with a fixed ridge thickness $W = 0.12R$.

We can conclude from the figure: for a fixed ridge thickness W, the wave numbers of TE_{11} and TE_{21L} modes are still mainly determined by the ridge gap d, which is similar to those of a general quadruple ridged circular waveguide as mentioned in [14]. With decreasing the edge width W_c, the cutoff wave number of dominant TE_{11} decreases continuously, because the total length of the ridge is increased, while
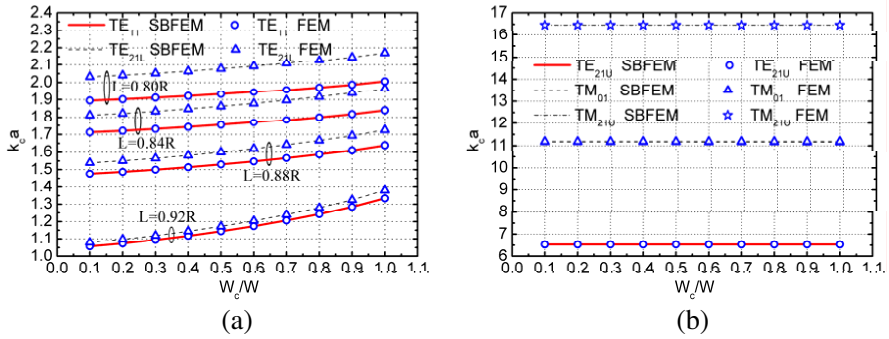
Figure 5. Normalized wave numbers versus the L and W_c. (a) TE_{11} and TE_{21L} modes and (b) TE_{21U}, TM_{01} and TM_{12U} modes.

that of TE_{21U} keeps almost stable, which then can broad the single bandwidth if the TE_{21L} mode is sufficiently suppressed or not excited. There are also TM_{01} and TM_{21U} modes, whose wave numbers stay almost unchanged. It is clear that edge width W_c has influence mainly on the TE_{11} and TE_{21L} modes while little influence on other higher modes when the ridges are heavily loaded.

In a conventional quadruple ridge waveguide design, the ridge thickness W should be less than the gap distance d. However, there is no such limitation with the quadruple corner-cut ridged circular waveguide. Therefore, the effect of the ridge thickness W also with gap distance d for a fixed edge width $W_c = 0.08R$ is investigated over a wider range, as shown in Figures 6 and 7. The main results from the figures are as follows.

(1) As to TE modes shown in Figure 6, we can achieve:

(a) The normalized wave numbers of TE_{11}, TE_{21L} modes are still mainly determined by the ridge gap d. Those of TE_{11}, TE_{21L} modes decrease at the beginning then increase as W increases. Meanwhile, they have nearly the same value when the ridge gap $d = 0.10R$ and $d = 0.20R$, and a larger ridge thickness W has little effect on them for $d = 0.10R$.

(b) The normalized wave number of TE_{21U} mode is influenced by both d and W while d has little influence on it with $W/W_c \leq 3$. It increases at the beginning then decreases as W increases.

(c) The normalized wave numbers of TE_{31} and TE_{01} modes are mainly determined by W when $W/W_c \leq 7.5$ for TE_{31} modes and $W/W_c \leq 8.5$ for TE_{01} mode. They also increase continuously as W increases then decrease after $W/W_c > 7.5$ and $W/W_c > 8.5$ for the TE_{31} and TE_{01} modes respectively.

(2) As to the TM modes shown in Figure 7, we can obtain:

(a) When $d \leq 0.20R$, the normalized wave numbers of all the TM_{01}, TE_{11}, TE_{21L}, TE_{21U} and TE_{31} modes are mainly determined by W and increase gradually as W/W_c increases. The wave numbers of TM_{01}, TE_{11}, TE_{21L} and TE_{31} modes for $d = 0.40R$ are very close to those for $d \leq 0.20R$. However, those of TM_{01} and TE_{31} modes for $d = 0.40R$ tend to flat after $W/W_c \geq 9$ and $W/W_c \geq 8.5$ respectively.

(b) When W/W_c increases, the normalized wave numbers of TM_{01} and TE_{31} modes for $d = 0.60R$ increase at the beginning then tend to flat especially for TM_{01} mode, while those of TM_{11} and TE_{20L} modes increase continuously.

(c) The normalized wave number of TE_{21U} mode is influenced by both d and W when $d > 0.20R$.

Since TE_{11} mode is close to TE_{21L} mode in wave number, the relative single-mode bandwidth is then determined by the wave
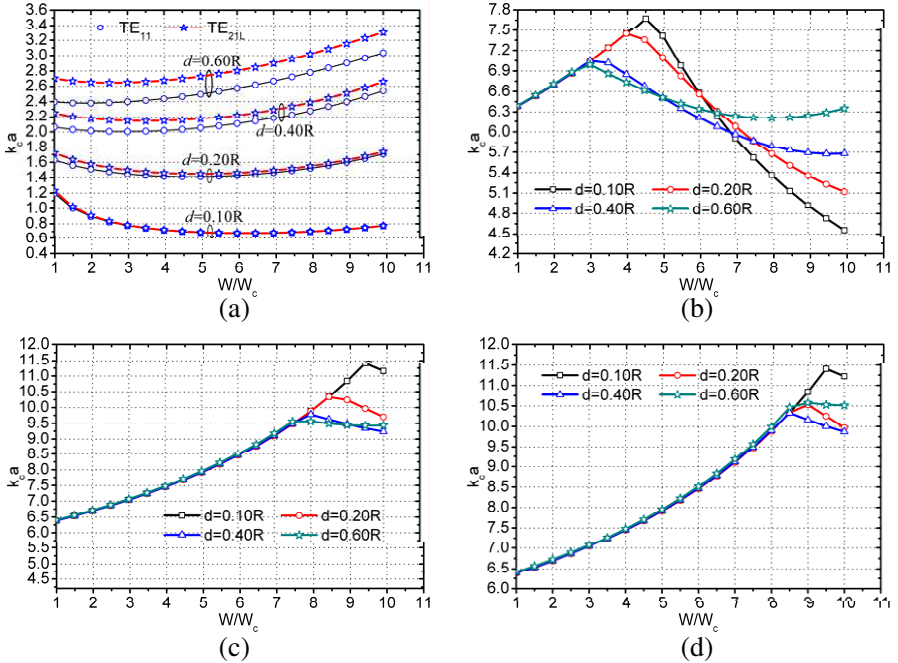
Figure 6. Normalized wave numbers versus the d and W for TE modes. (a) TE_{11} and TE_{21L} modes, (b) TE_{21U} mode, (c) TE_{31} mode and (d) TE_{01} mode.
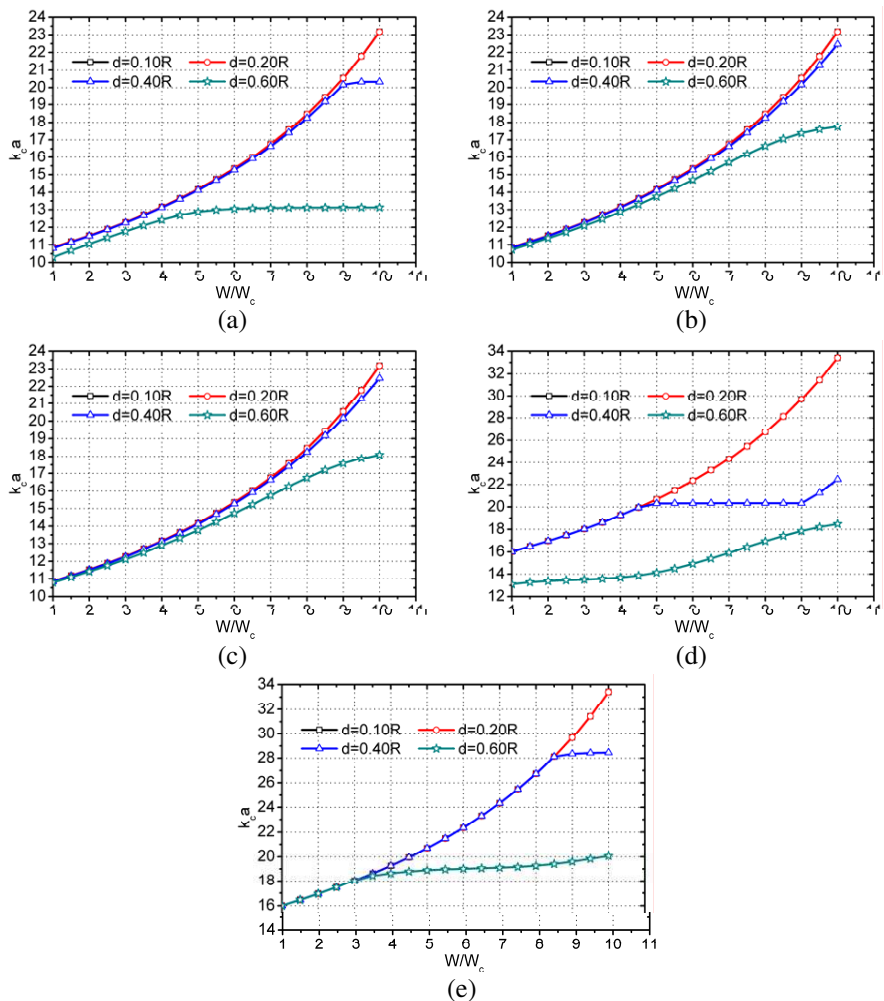
Figure 7. Normalized cutoff wave numbers versus the d and W for TM modes. (a) TM_{01} mode, (b) TM_{11} mode, (c) TM_{21L} mode, (d) TM_{21U} mode and (e) TM_{31} mode.

numbers of the TE_{11} and TE_{21U} modes if TE_{21L} mode is sufficiently suppressed or not excited. Certainly, the relative single-mode bandwidth between the former symmetry modes (TE_{11} and TE_{31} modes) may be also considered. The calculation formula of single-
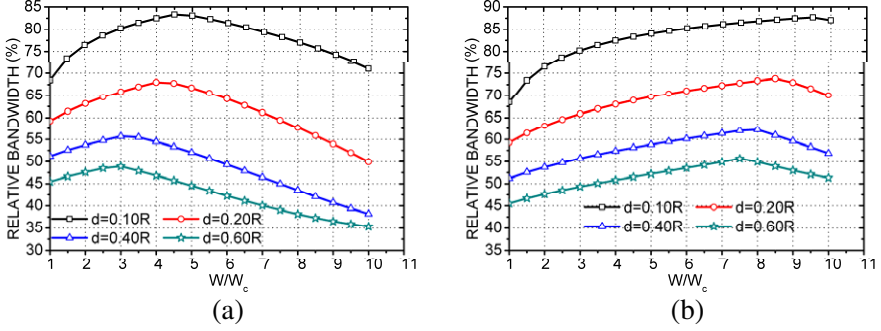
Figure 8. Single-mode bandwidth of a quadruple corner-cut ridged square waveguide (a) TE_{11} and TE_{21U} modes and (b) TE_{11} and TE_{31} modes.

mode bandwidth is defined as follows:

$$BW = \frac{\left(k_c^{TE_2} - k_c^{TE_1}\right)}{\left(k_c^{TE_2} + k_c^{TE_1}\right)} \times 100\%.$$

where TE_1 and TE_2 represent lower and higher modes, respectively.

As shown in Figure 8, the bandwidths are also mainly determined by gap distance d and ridge thickness W. For the single-mode bandwidth between TE_{11} and TE_{21U} modes, the bandwidth increases first then decreases as W/W_c increases, while for the single-mode bandwidth between TE_{11} and TE_{31} modes, it decreases continuously except for extraordinarily large W/W_c as W/W_c increases. An optimal bandwidth can be obtained by tuning the ridge thickness W, corner-cut edge width W_c and ridge gap d.

5. CONCLUSION

The semi-analytical SBFEM has been successfully applied to analyze the quadruple corner-cut ridged circular waveguides. High rate of convergence, high efficiency, excellent accuracy, less amount of computation time and much less nodes discretized on the boundary in the SBFEM are observed in the numerical examples, and the singularity problem can be easily solved. The wave numbers of several lowest modes for both TE and TM cases are examined in detail. The main results conclude as follows: (1) When the ratio $(2R - d)/(2R)$ increases with a fixed ridge thickness W, the normalized wave numbers of TE_{11} and TE_{21L} and all the TM modes increase; the TE_{21L} mode has a wave number very close to that of TE_{11} mode; those of the

TE_{21U}, TE_{01} and TE_{31} modes tend to the same value; and those of TM_{01}, TM_{11} and TM_{21L} modes tend to the same value and those of TM_{21U}, TM_{31} and TM_{02} modes have a nearly same value. (2) The wave numbers of TE_{11} and TE_{21L} modes are mainly determined by the ridge gap d. With decreasing the edge width W_c for a fixed ridge thickness W, the cutoff wave number of dominant TE_{11} decreases continuously while that of TE_{21U} keeps almost stable, which then can broaden the single bandwidth. There are also TM_{01} and TM_{21U} modes, whose wave numbers stay almost unchanged. (3) For a fixed edge width W_c, the normalized wave numbers of TE_{11}, TE_{21L} modes are still mainly determined by the ridge gap d. That of TE_{21U} mode is influenced by both d and W, while d has little influence on it with $W/W_c \le 3$. The normalized wave numbers of TE_{31} and TE_{01} modes are mainly determined by W when $W/W_c \le 7.5$. When $d \le 0.20R$. The normalized wave numbers of all the TM_{01}, TE_{11}, TE_{21L}, TE_{21U} and TE_{31} modes are mainly determined by W. The normalized wave number of TE_{21U} mode is influenced by both d and W when $d > 0.20R$. Meanwhile, the single-mode bandwidth has been evaluated to examine the effect of cut-corners, and an optimal bandwidth can be obtained by tuning the ridge thickness W, corner-cut edge width W_c and ridge gap d.

ACKNOWLEDGMENT

REFERENCES

1. Cohn, S. B., "Properties of ridge waveguide," *Proceedings of the IRE*, Vol. 35, 783–788, 1947.
2. Hopfer, S., "The design of ridged waveguides," *IEEE Trans. Microwave Theory Tech.*, Vol. 3, No. 10, 20–29, 1955.
3. Rong, Y. and K. A. Zak, "Characteristics of generalized rectangular and circular ridge waveguides," *IEEE Trans. Microwave Theory Tech.*, Vol. 48, No. 2, 258–265, 2000.
4. Tsandoulas, G. N. and G. H. Knittel, "The analysis and design of dualpolarization square-waveguide phased arrays," *IEEE Transactions on Antennas and Propagation*, Vol. 21, No. 6, 796–808,1973.
5. De Villiers, D. I. L., P. Meyer and K D Palmer, "Broadband

offset quad-ridged waveguide orthomode transducer," *Electronics Letters*, Vol. 45, No. 1, 60–62, 2009

6. Ding, S., B. Jia, F. Li, and Z. Zhu, "3D simulation of 18-vane 5.8 GHz magnetron," *Journal of Electromagnetic Waves and Applications*, Vol. 22, No. 14–15, 1925–1930, 2008.

7. Singh, K., P. K. Jain, and B. N. Basu, "Analysis of a coaxial waveguide corrugated with wedge-shaped radial vanes considering azimuthal harmonic effects," *Progress In Electromagnetics Research*, Vol. 47, 297–312, 2004.

8. Singh, K., P. K. Jain, and B. N. Basu. "Analysis of a corrugated coaxial waveguide resonator for mode rarefaction in a gyrotron," *IEEE Trans. Plasma Science*, Vol. 33, 1024–1030, 2005.

9. Barroso, J. J., R. A. Correa, and P. J. de Castro, "Gyrotron coaxial cylindrical resonators with corrugated inner conductor: Theory and experiment," *IEEE Trans. Microwave Theory Tech.*, Vol. 46, No. 9, 1221–1230, 1998.

10. Iatrou, C. T., S. Kern, and A. B. Pavelyev, "Coaxial cavities with corrugated inner conductor for gyrotrons," *IEEE Trans. Microwave Theory Tech.*, Vol. 44, No. 1, 56–64, Jan. 1996.

11. Agrawal, M., G. Singh, P. K. Jain, and B. N. Basu, "Analysis of tapered vane-loaded structures for broadband gyro-TWTs," *IEEE Trans. Plasma Science,* Vol. 29, 439–444, 2001.

12. Qiu, C. R., Z. B. Ouyang, S. C. Zhang, H. B. Zhang, and J. B. Jin, "Self-consistent nonlinear investigation of an outer-slotted-coaxial waveguide gyrotron traveling-wave amplifier," *IEEE Trans. Plasma Science*, Vol. 33, No. 3, 1013–1018, 2005.

13. Chen, M. H., G. N. Tsandoulas, and F. G. Willwerth, "Modal characteristics of quadruple-ridged circular and square waveguides," *IEEE Trans. Microwave Theory Tech.*, Vol. 22, No. 8, 801–804, 1974.

14. Sun, W. and C. A. Balanis, "Analysis and design of quadruple-ridged waveguides," *IEEE Trans. Microwave Theory Tech.*, Vol. 4, No. 12, 2201–2207, 1994.

15. Tang, Y., J. Zhao, and W. Wu, "Analysis of quadruple-ridged square waveguide by multilayer perceptron neural network model," *Asia-Pacific Microwave Conference, APMC 2006*, 1912–1918, 2006.

16. Tang, Y., J. Zhao, and W. Wu, "Mode-matching analysis of quadruple-ridged square waveguides," *Microwave and Optical Technology Letters*, Vol. 47, No. 2, 190–194, 2005.

17. Sexson, T., "Quadruply ridged hom," Tech. Rep., ECOM-018 1-M

1 160, Army Electronics Command., US, Mar. 1968.

18. Canatan, F., "Cutoff wavenumbers of ridged circular waveguides via Ritz-Galerkin approach," *Electronics Letters*, Vol. 25, 1036–1038, 1989.

19. Rong, Y., "The bandwidth characteristics of ridged circular waveguide," *Microwave and Optical Technology Letters*, Vol. 3, 347–350, 1990.

20. Zheng, Q., F. Xie, and B. Yao, ect., "Analysis of a ridge waveguide family based on subregion solution of multipole theory," *Automation Congress*, 1–4, WAC, World, 2008.

21. Skinner, S. J. and G. L. James, "Wide-band orthomode transducers," *IEEE Trans. Microwave Theory Tech.*, Vol. 39, No. 2, 294–300, 1991.

22. Schiff, B., "Eigenvalues for ridged and other waveguides containing corners of angle $3\pi/2$ or 2π by the finite element method," *IEEE Trans. Microwave Theory Tech.*, Vol. 39, No. 6, 1034–1039, 1991.

23. Song, C. H. and J. P. Wolf, "The scaled boundary finite-element method — Alias consistent infinitesimal finite-element cell method — For elastodynamics," *Computer Methods in Applied Mechanics and Engineering*, Vol. 147, 329–355, 1997.

24. Wolf, J. P. and C. M. Song, *The Scaled Boundary Finite Element Method*, Wiley Press, Chichester, England, 2003.

25. Liu, J., G. Lin, F. Wang, et al., "The scaled boundary finite element method applied to electromagnetic field problems," *IOP Conference Series: Materials Science and Engineering*, Vol. 10, No. 1, 2245, Syndey, Jul. 2010.

26. Song, C. M., "The scaled boundary finite element method in structural dynamics," *International Journal for Numerical Methods in Engineering*, Vol. 77, 1139–1171, 2009.

27. Deeks, A. J. and J. P. Wolf, "A virtual work derivation of the scaled boundary finite-element method for elastostatics," *Computational Mechanics*, Vol. 28, 489–504, 2002.

28. Hu, Z., G. Lin, Y. Wang, and J. Liu, "A hamiltonian-based derivation of scaled boundary finite element method for elasticity problems," *IOP Conference Series: Materials Science and Engineering*, Vol. 10, No. 1, 2213, Syndey, Jul. 2010.